

# Static and dynamic mechanical properties of wire and arc additively manufactured SS316L and ER70S6

Gleb Gil Goviazin<sup>a,b,\*</sup>, Amnon Shirizly<sup>a,b</sup>, Daniel Rittel<sup>a</sup>

<sup>a</sup> Faculty of Mechanical Engineering, Technion – Israel Institute of Technology, 32000, Haifa, Israel

<sup>b</sup> Rafael, POB 2250 (774), Haifa, 3102102, Israel

## ARTICLE INFO

### Keywords:

Wire and arc additive manufacturing (WAAM)  
SS316L  
ER70S6  
Shear compression specimen (SCS)  
Shear tension specimen (STS)

## ABSTRACT

The worldwide growing demand for additive manufacturing (AM) has led to the development of wire and arc additive manufacturing (WAAM) technique. In this work, SS316L and ER70S6 thick-walled cylinders were produced, and specimens were extracted in the as fabricated condition. For comparison, bulk SS316L and AISI 1020 specimens were machined from cold drawn (also in as received condition) bars and tested accordingly. Four types of specimens were used: “dog-bone” for tension, cylinder for compression, shear tension specimen (STS) and shear compression specimen (SCS) for both mixed shear tension and shear compression loading, respectively. Experiments were carried out under static (ca.  $10^{-3}$  1/s) and dynamic conditions (from  $10^2$  to  $10^4$  1/s). WAAM SS316L SCS under static conditions, and WAAM cylinder under dynamic loading showed a unique stress-strain curvature (hardening) that was not observed for the bulk material. By contrast, WAAM ER70S6 material shows somewhat similar properties to those of AISI 1020, indicating it might be a suitable candidate for repair or even material replacement for AISI 1020 as a material for AM products.

## 1. Introduction

Additive Manufacturing (AM) processes have become a common manufacturing technology over the last decade, most suitable for high complexity geometries and low quantities (Ding et al., 2015). Under the term of AM for metals one finds several classifications as: powder bed fusion, direct energy deposition, binder jetting and sheet lamination which may use metal powder, metal wire and metal foil as raw material, depending on the chosen AM process. Each classification has some subclassifications, e.g., direct energy deposition has electron beam freeform fabrication (EBF), wire and arc additive manufacturing (WAAM) etc. Under the previous subclassifications one finds additional refinements, describing the technology used in the process. Such refinements for example, can be found in WAAM. WAAM can be done by gas tungsten arc welding (GTAW) or gas metal arc welding (GMAW), when the first is slower but more accurate than the second. When using a WAAM process one should plan and optimize the electrodes' path and other parameters to produce the desired products with high repeatability. Those parameters include direction of wire feeding (front, back or side), bead width and distance between each pair of beads, oscillations of the welding head and many other parameters as in (Ding et al.,

2011; Liberini et al., 2017).

The many cycles of layer-by-layer deposition, as in WAAM, cause complex thermal histories that differ from those characterizing conventional manufacturing procedures. As a result, the mechanical properties of AM products in general, and WAAM in particular, might be different from those of a bulk (conventionally manufactured) material, and indeed, such differences have been reported for some materials e.g., Inconel 625, Ti-6Al-4V, austenitic stainless steel like SS316L (Beese, 2018; Ni et al., 2019; Pham et al., 2017). Hence, after optimizing the AM/WAAM parameters to achieve the desired geometry, a full characterization of the mechanical properties is desirable in the part's working regime, for the specific manufacturing procedure. Furthermore, the direction of applied load with respect to the layering direction, affects the mechanical properties too (Tolosa et al., 2010; Wu et al., 2019). According to this, one should not rely on mechanical properties extracted from a different type of AM (EBF compared to WAAM for example). One should also verify the mechanical properties for the same type of AM process, but loaded or made under different conditions (for WAAM process, e.g., different current supply, wire feed velocity etc.). Usually, works done on mechanical behavior of AM products, concentrate on their microstructure and static behavior, see e.g., (Beese, 2018; Tolosa

\* Corresponding author. Faculty of Mechanical Engineering, Technion – Israel Institute of Technology, 32000, Haifa, Israel.

E-mail addresses: [gil.goviazin@gmail.com](mailto:gil.goviazin@gmail.com) (G.G. Goviazin), [a.shirizly@gmail.com](mailto:a.shirizly@gmail.com) (A. Shirizly), [merittel@me.technion.ac.il](mailto:merittel@me.technion.ac.il) (D. Rittel).

et al., 2010; Wu et al., 2019), while only a few of those works examined the high strain rate regime (Fadida et al., 2015). Even fewer works examined mixed loading conditions (some degree of triaxiality) (Fadida et al., 2019), which might have an impact on the stress-strain relation and failure characteristics of the material (Bai and Wierzbicki, 2008; Gao et al., 2009; Pivonka and Willam, 2003).

In this article we investigate the mechanical behavior of specimens, machined from as manufactured thick-walled cylinders, all perpendicular to the layering orientation. These cylinders were produced by WAAM process from SS316L and ER70S6 wires. The cylinders were taken from a previous work of Shirizly and Dolev (2019), whose emphasis was on static tension behavior alone, and the WAAM parameters were established there. Further investigation concentrating on stress corrosion and corrosion fatigue was carried out on those same cylinders (Ron et al., 2019, 2020, 2021) and showed a very good behavior compared to their bulk materials. The present work concentrates on large strain mechanical behavior of the materials under static and dynamic loading, which is highly important for accurate modeling of machining, plastic forming, plastic fracture, high speed impact and penetration. Both static ( $\sim 10^{-3}$  [1/s]) and dynamic ( $\sim 10^3$  [1/s]) experiments, were performed by tension, compression, shear-compression (SCS) (Dorogoy et al., 2015) and shear-tension (STS) (Dorogoy et al., 2016) specimens for both materials. For the sake of comparison, the same tests were carried out on bulk (extruded) material of SS316L, and 1020 (closest available to ER70S-6 as bulk material) 10 mm diameter cold drawn rods were machined to the same specimens' geometry and compared to the WAAM specimens. AM materials show improved mechanical behavior with respect to annealed bulk material (Ni et al., 2019; Pham et al., 2017; Shirizly and Dolev, 2019).

The article is organized as follows: section 2 describes the specimens' preparation procedures according to layering orientation and geometries of the different specimens, experimental procedures and summarized too. The necessary background on SCS and STS specimens is given in section 3 with a new method to overcome machining tolerances errors in these specimens. For completeness of section 3, the simulation procedure is described. Section 4 reports the experimental results, followed by a discussion section in sections 5. Finally, the main conclusions of this study are presented in section 6.

## 2. Specimens' preparations, types, and experimental procedure

WAAM specimens were machined from a thick-walled cylinder with 15 mm wall thickness, 95 mm inner radii and 120 mm height, layering orientation (for WAAM specimens) is perpendicular to the longitudinal axis as shown in Fig. 1. Bulk material's specimens were machined from a 10 [mm] rods. All specimens' geometry, and dimensions are shown in Fig. 2.

Static and dynamic, tension and compression, tests were made using commonly used specimens as dog-bone and cylinder. Hence these

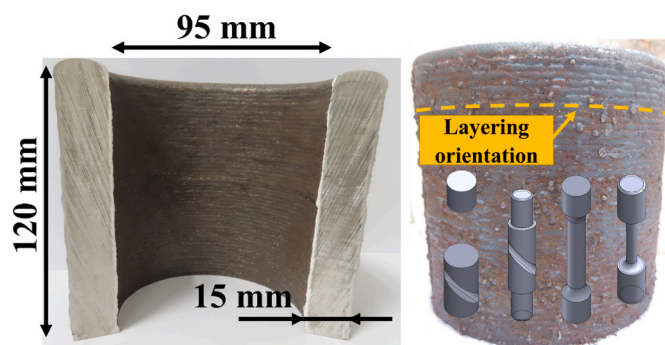


Fig. 1. Typical thick-walled cylinder made by WAAM. Deposition layers' direction and specimens' orientations are indicated.

specimens do not need any further introduction.

Mixed mode static and dynamic experiments, such as, shear-tension and shear-compression experiments were made using STS and SCS. These specimens were developed by Rittel et al. and later modified by Dorogoy et al. (Dorogoy et al., 2015, 2016; Rittel et al., 2002a). Those specimens were made for the investigation of materials undergoing large equivalent plastic strain (as the main concern of this work), and for a wide range of equivalent strain rates. Both specimens have two diametrically opposed circular slots, machined at  $45^\circ$  to the longitudinal axis. The difference between STS and SCS is screw or flat ends as presented in Fig. 2 (d) and (e), respectively.

Experiments in the static region were done using a servo-hydraulic MTS machine, with a crosshead speed adjusted to insure strain rate of about  $10^{-3}$  1/s for all specimens, according to their geometry. Forces were measured using the MTS load cell, while optical laser extensometer was used to measure the vertical displacement. The experiments were stopped when the specimens deformed significantly (e.g., barreling for cylinders, necking or broke). All presented results show the equivalent true stress strain curves up to the ultimate equivalent stress point (UTS).

Experiments in the dynamic region were done using a hardened C300 Maraging steel split-Hopkinson bar (Kolsky bar) (Kolsky, 1953; Weinong Chen, 2013), with a diameter of 19.05 mm for compression and 12.7 mm for tension. All shots were done under 3 bar over pressure, which resulted in a  $\sim 27$  m/s striker velocity in compression, and  $\sim 10$  m/s in tension so that the resulting strain rate was in the range of  $10^2$  to  $10^4$  1/s, depending on the specific specimen tested. The signals from the incident and transmitted bars' strain gauges were recorded using a Nicolet 440–12-bit differential oscilloscope.

Although large differences can be seen between the bulk and WAAM manufacturing methods for both materials, each material exhibits a good agreement between its different specimens.

## 3. Numerical and experimental overview

### 3.1. SCS and STS data reduction

Shear-compression specimen (SCS) was first introduced by Rittel et al. (Rittel et al., 2002a). and has been used in several research since then, e.g., (Dorogoy and Rittel, 2017; Rittel et al., 2002b; Vural et al., 2003). Full representation of data extraction process for the modified SCS and shear tension specimen (STS) can be found in (Dorogoy et al., 2015, 2016), while the validation of those specimens was shown in (Dorogoy and Rittel, 2005a,b). Hence, we will only review the basic guidelines here.

In general, the analysis is hybrid and combines experimental results with finite elements (FE) simulations. The steps one needs to take to analyze these specimens are:

1. Make a first guess for the specimen's equivalent stress-strain relation. This can be done by using literature or tension/compression experiments using "dog-bone"/cylinder specimens, respectively.
2. Simulate SCS/STS under the same equivalent strain rate and use the first guess of the equivalent stress-strain relation.
3. Use the simulated data to achieve the fitting parameters ( $k_i$ ) from the following equations, once more for more detailed information the reader is kindly referred to (Dorogoy et al., 2015, 2016):

$$\hat{\epsilon}_p = \sum_{i=1}^N k_{i+2} \left( \frac{d - d_i}{h} \right)^i \quad \text{for } d > d_y \quad (1)$$

$$\hat{\sigma} = k_1 (1 - k_2 \hat{\epsilon}_p) \frac{P}{D \cdot t} \quad \text{for } P > P_y \quad (2)$$

When:

$k_i$  – fitting parameters.

$d, d_y$  – specimen's displacement during simulation and the

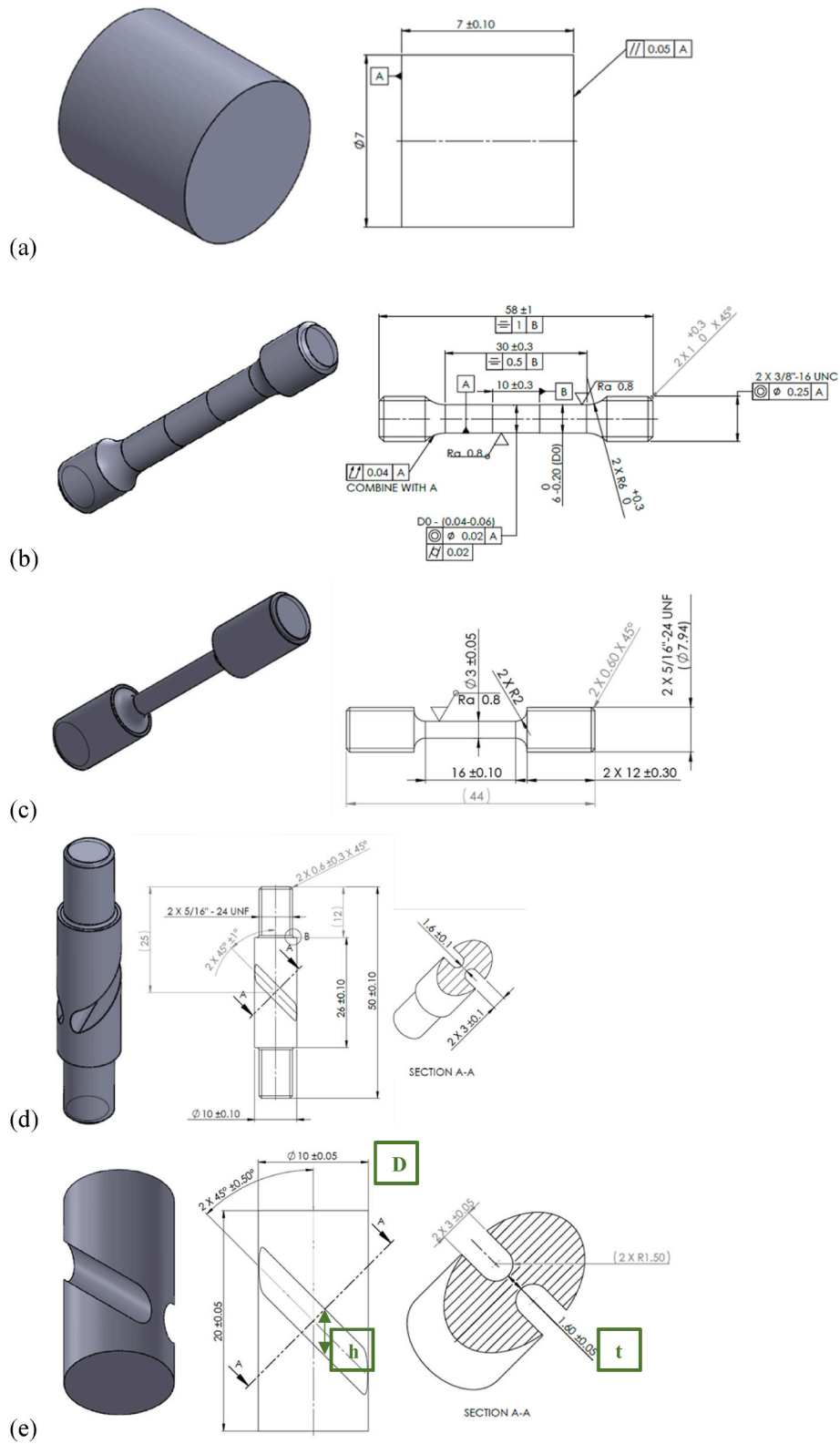


**Fig. 2.** All specimens' geometry. (a) cylinder for static and dynamic compression experiments. (b) dog-bone for static tension experiments. (c) dog-bone for dynamic tension experiments. (d) STS (shear tension) for static and dynamic shear-tension experiments. (e) SCS (shear compression) for static and dynamic shear-compression experiments.

displacement at the yield point, respectively.

$P$ ,  $P_y$  – force used during the simulation and yield load, respectively.

$D$ ,  $t$ ,  $h$  – specimen's total diameter, gauge thickness and gauge height, see Fig. 2e.

$\hat{\epsilon}_p$ ,  $\hat{\sigma}$  – equivalent plastic strain and corresponding equivalent stress. The simulated  $P$ ,  $d$ ,  $\hat{\epsilon}_p$ ,  $\hat{\sigma}$  are used to obtain  $k_i$ .

4. Using the obtained  $k_i$ , force and displacements from the experimental data, and equations (1) and (2) will construct the right equivalent stress – strain curve for the experiment. Use this equivalent stress – strain relation to simulate once more the SCS/STS.
5. Compare the resulting force – displacement curve of the SCS/STS from the simulation to the experimental one (if more than one specimen was tested, use the average result of all experiments tested under those conditions with the specific specimen's geometry). For dynamic experiments you may compare the simulated longitudinal strains in the incident and transmitted bars instead of force – displacement of the specimen since force and displacement are derived from the strain measurements as was demonstrated by Kolsky (1953).
6. If a deviation exists between the experimental and simulated force – displacement curves (or strains for dynamic tests), iterate until convergence. The word iterate means that one needs to update the assumed stress – strain relation according to the comparison between the simulated and experimental force – displacement curve until convergence is obtained.

### 3.2. A new method for force factor correction

Simulations regarding SCS and STS are usually done with their *nominal dimensions* without considering the actual gauge dimensions which might differ due to manufacturing tolerances. To the best of our knowledge, none of the previous works done with SCS/STS dealt with this issue.

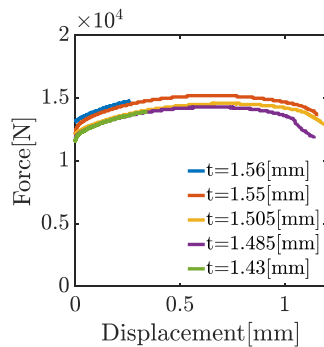
Analyzing the most influencing dimensions from equation (1), one can deduce that the gauge's height ( $h$ ) is very important for the correctness of the strain. This dimension is achieved using a standard 3 mm machining tool and doesn't depend on the operator which make it very accurate. Hence, no special treatment is needed.

According to equation (2), the diameter ( $D$ ) and gauge thickness ( $t$ ) are important for the correctness of the stress. On the one hand, the diameter has a large value (10 mm) and is an outside diameter which is easy to maintain. On the other hand, the nominal gauge thickness (indicated as “ $t$ ” in Fig. 2e) is 1.6 mm, which is small related to other specimens like “dog-bone” (6- and 3-mm cross section in this paper for static and dynamic specimens in this work, respectively) and has a geometry that is much harder to machine, a fact that may lead to larger dimensional imperfections, resulting in some inaccuracy in the equivalent stress – strain relation deduced from the data reduction process.

Consequently, the force will be corrected by a factor which equals the nominal gauge thickness ( $t_{nominal}$ ) divided by its measured specific thickness ( $t_{actual}$ ), as shown in equation (3), and illustrated in Fig. 3.

$$F_{corrected} = F_{experimental} \frac{t_{nominal}}{t_{actual}} \quad (3)$$

Force - Displacement for Bulk SS316L Static STS Specimen - Before Correction



To further illustrate the importance of such a force correction, representative equivalent strain-stress curves are presented Fig. 4. It can be noted that after correcting the force component, the equivalent stress-strain curves of the STS and the dog bone specimen are in excellent agreement. Throughout this work, the same correction was applied to both static and dynamic shear experiments.

### 3.3. Numerical simulations

All the simulations were carried out using the commercial final element package ABAQUS (ABAQUS, 2014) according to the guidelines established in (Dorogoy et al., 2015, 2016). The more conventional specimens, like “dog-bone” and cylinders, were analyzed analytically as usually done for static and dynamic (Kolsky bar) experiments (Kolsky,

## True Stress Vs. Plastic Strain - Force correction effect

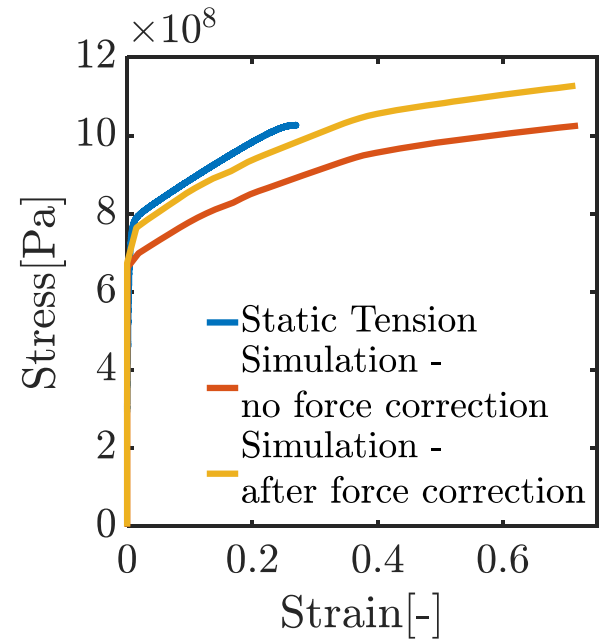


Fig. 4. True equivalent stress Vs. true plastic strain for static tension (dog-bone), and static STS before and after force correction experiments on Bulk SS316L. The expected good agreement between the tension and STS specimens can be seen after force correction only. Correct plastic in title.

Force - Displacement for Bulk SS316L Static STS Specimen - After Correction

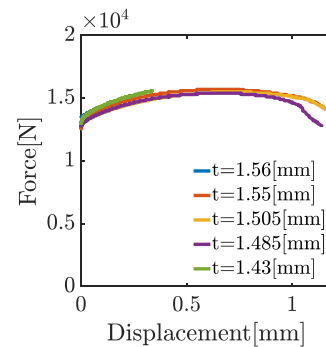


Fig. 3. Static STS with 316L bulk material, force – displacement curves, before and after force correction due to manufacturing tolerances. After correction there is a much better agreement between the curves. Gauges' thickness is reported in the legend.



1953), while the SCS and STS have to be analyzed in a hybrid manner by experiments, calculations and simulations.

Using the inherent symmetry of the specimens (SCS and STS) only a half problem was modelled using a symmetry plane along the longitudinal axis. The specimens were meshed using hexahedral, linear, reduced integration elements (C3D8R type in ABAQUS notation) with a seed of 0.5 mm. To avoid hourglass problems the gauge area was meshed using hexahedral, linear elements (C3D8) with a seed of 0.2 mm. The front, side, and back views of a meshed SCS are shown in Fig. 5. Static experiments were simulated using implicit solution scheme while dynamic simulations were done using the explicit solution scheme due to the importance of wave propagation in dynamic experiments.

Static (implicit) SCS modelling was done by fixing a single node at the center of the bottom face and using a symmetry plane at the bottom face of the specimen to model the stationary side of the MTS machine in the experiment. This symmetry condition was applied in addition to the symmetry plane of the half problem discussed above, Fig. 5. A vertical displacement corresponding to the one enforced and measured during the specific experiment was applied.

Static STS specimens were modelled using a fixed (“encastre”) boundary condition on one side of the specimen’s “threads”, while a vertical displacement was applied to the other side “treads” according to the one measured during the corresponding experiment, as presented in Fig. 6, simulating the exact boundary conditions as they were during the experiment. Once again, a symmetry plane was used for the sectioned face alone for the STS. Finally, the force – displacement curves from the simulations were compared to the experimental one, the simulation was repeated (iterated) until good agreement was achieved between those curves, as presented in Fig. 7. This good agreement between the simulated and experimental force-displacement curves indicates that the equivalent stress – strain relation for the material was found.

Unlike the static simulations where only the specimen was modelled, in dynamic (explicit) simulations the specimen (SCS or STS), and the bars of the Kolsky bar apparatus were modelled too. Specimens’ meshing was identical to that of the static simulations, and the bars were meshed using a seed of 2 mm (1 mm seed was tested too and no difference was found). Like before, due to the symmetry of the problem only half a problem was modelled along the longitudinal direction. A velocity profile boundary condition was applied to the incident bar according to the experimental one at the striker’s end, and the longitudinal strains in the incident and transmitted bars were taken from the

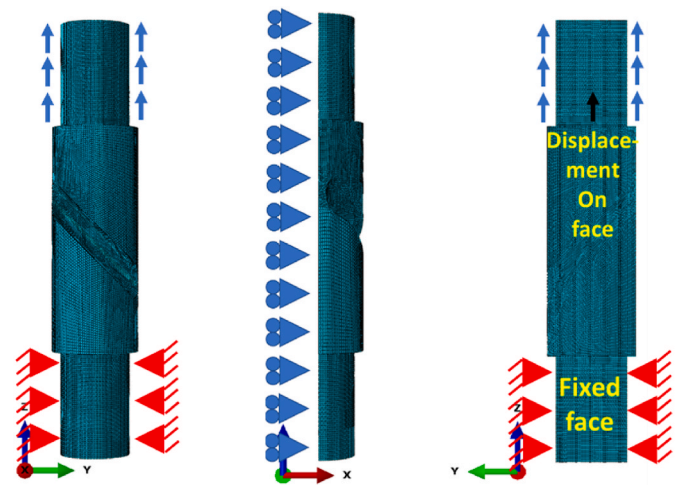


Fig. 6. (Left to right) The front, side, and back views of a meshed STS with boundary conditions for a static (implicit) solution. Symmetry was applied to the sectioned surface (side view) to model the hole problem. “Treads” on one side were fixed. Displacement was applied to the “threads” of the other side according to the measured one.

simulation at identical positions along the bars as on the experimental bars. The STS were bolted into the incident and transmitted bars during the tension experiments. This threaded area was modelled without threads, but in order to simulate the bonding between the specimen and the bars, merged nodes between the specimen’s and bars’ threads were used.

Finally, the incident, reflected, and transmitted pulses were compared to the experimental ones, and iterations were carried out until a good agreement was achieved, as shown in Fig. 8.

### 3.4. Experimental

All the types of specimens presented in Fig. 2 were investigated for both WAAM material and bulk material, for both SS316L and ER70S6. Four static and four dynamic experiments were carried out (dog-bone, cylinder, SCS, STS). A minimum of three repetitive static experiments were done for each specimen kind, and a minimum of five dynamic

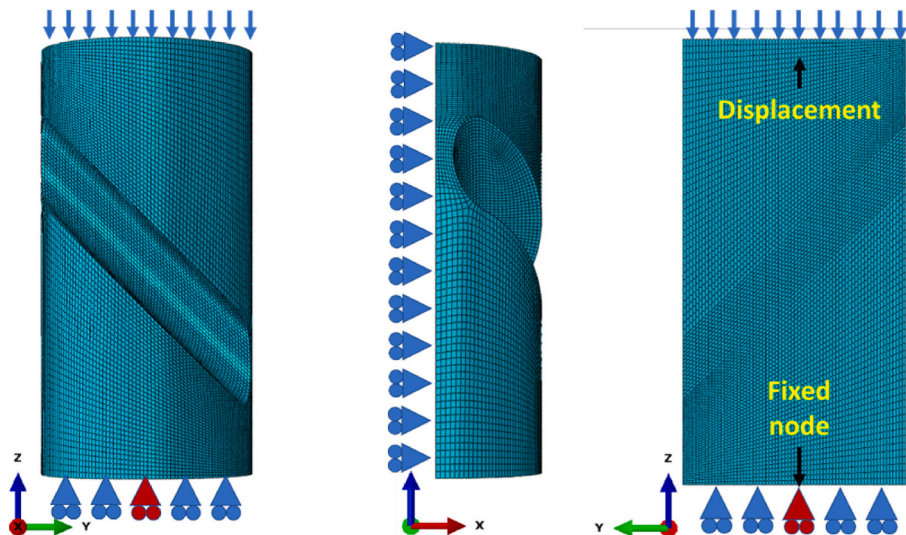


Fig. 5. (Left to right) The front, side, and back views of a meshed SCS with boundary conditions for a static (implicit) solution. Symmetry was applied to the sectioned surface (side view) to model the hole problem. Symmetry was also applied to the bottom face, to indicate the stationary side of the MTS machine, one node was fixed to prevent numerical stability problems. Displacement was applied to the top face according to the measured one.

## Force Vs. Displacement - Experimental and simulated

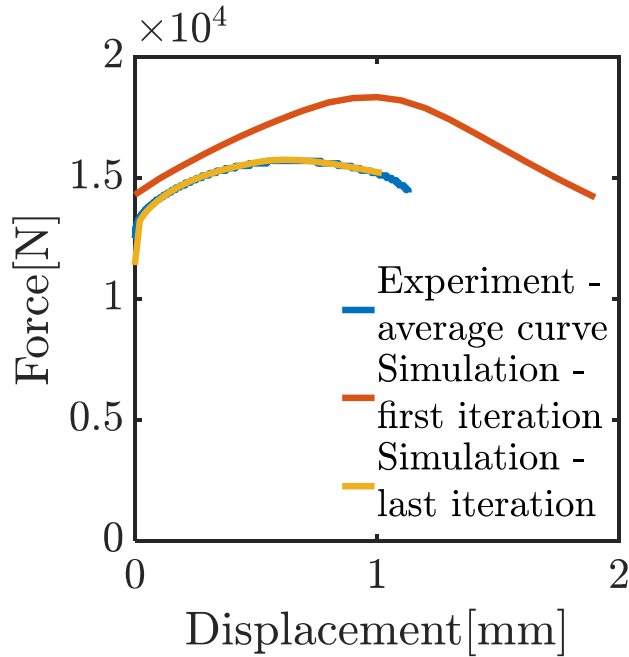


Fig. 7. Force – displacement curves of static STS with bulk SS316L. The curves stand for the experimental conditions, simulation after first iteration, and the final relation achieved after calibration. Big differences can be seen which are eliminated after convergence was achieved.

experiments for each specimen kind.

Dog-bone for static tension (Fig. 2 (b)), compression cylinder (Fig. 2 (a)), STS (Fig. 2 (d)) and SCS (Fig. 2 (e)) specimens were tested under a strain rate of about  $10^{-3}$  1/s (static conditions).

Dog-bone for dynamic tension (as seen in Fig. 2c), cylinder compression, STS and SCS specimens were tested with the same striking velocity (one for compression and one for tension) which was achieved by a constant overpressure of 3 bars in each experiment. This overpressure led to a variety of strain rates from  $10^2$  to  $10^4$  1/s depending on the specific experiment/specimen.

Finally, note that for tensile tests, results are presented as true stress-strain curves, so that processing is interrupted at the onset of necking. Likewise, static compression strains are limited to ca. 0.2 which corresponds to the onset of barreling. Such limitations do not exist for the combined shear test specimens.

## 4. Results

### 4.1. Static loading experiments

#### 4.1.1. WAAM and bulk SS316L

The results for all static SS316L (WAAM and bulk) experiments are presented in Fig. 9 and are summarized in appendix A. WAAM tension test shows some small deviation from the compression test (error bars are not presented since deviations of less than 5% were achieved), although they share the same equivalent yield stress. Cylinder, SCS and STS specimens exhibit a similar behavior up to 0.2 equivalent strain. The SCS for the WAAM material presents an unusual behavior for face-centered-cubic (FCC) metal that was not observed with the cylinder specimen due to barreling limitations. Namely, past 0.2 equivalent strain there is a change in the material's strain hardening as the curve exhibits an upward concavity. This type of behavior has been reported for hexagonal-closed-pack (HCP) materials like titanium (Ti) (Rittel et al., 2017) and magnesium (Mg) (Ali, 2012), but not for the current material made by WAAM.

Unlike the WAAM material, the bulk material has a similar behavior for all specimens up to 0.3 equivalent strain. Little difference is observed between the STS and SCS specimens for large equivalent strain (above 0.4).

#### 4.1.2. WAAM ER70S6 and bulk AISI 1020

All the results are presented in Fig. 10 and are summarized in appendix A. As before, a good agreement can be seen between different specimens of the same material. Although, small difference can be observed between the compression and tension results for WAAM material.

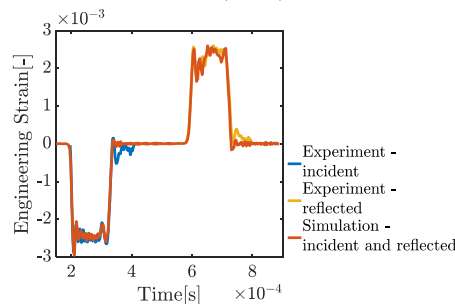
At the beginning the selected bulk material (cold drawn) has much larger yield and equivalent flow stresses than the WAAM material (same as SS316L), after an equivalent strain of about 0.3 the equivalent flow stress for WAAM and bulk materials becomes quite close and even almost the same for the STS specimens due to different strain hardening slopes at the beginning. This agreement at high equivalent strains was revealed with the SCS and STS specimens due to their capability to achieve high equivalent strains.

### 4.2. Dynamic loading experiments

#### 4.2.1. WAAM and bulk SS316L

The dynamic tests' results are presented in Fig. 11 and are summarized in appendix A. For the WAAM material, tension, SCS and STS results show an approximately linear hardening. By contrast, the compression specimens show kind of "S shape" behavior made of 3 linear segments (primarily bilinear with a small extension above 0.37 equivalent strain) which changes its initial slope at around an equivalent strain of 0.25. Interestingly, this same behavior was observed for the SCS during the static experiments and was discussed before. Both dynamic

Incident and Reflected Pulse (strain) Vs. Time



Transmitted Pulse (strain) Vs. Time

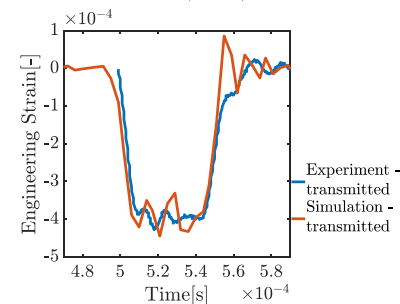
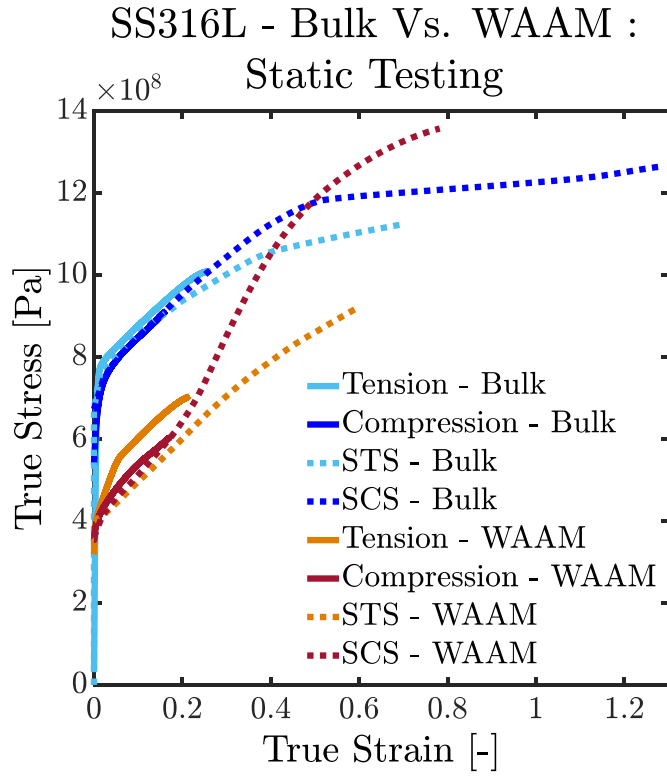
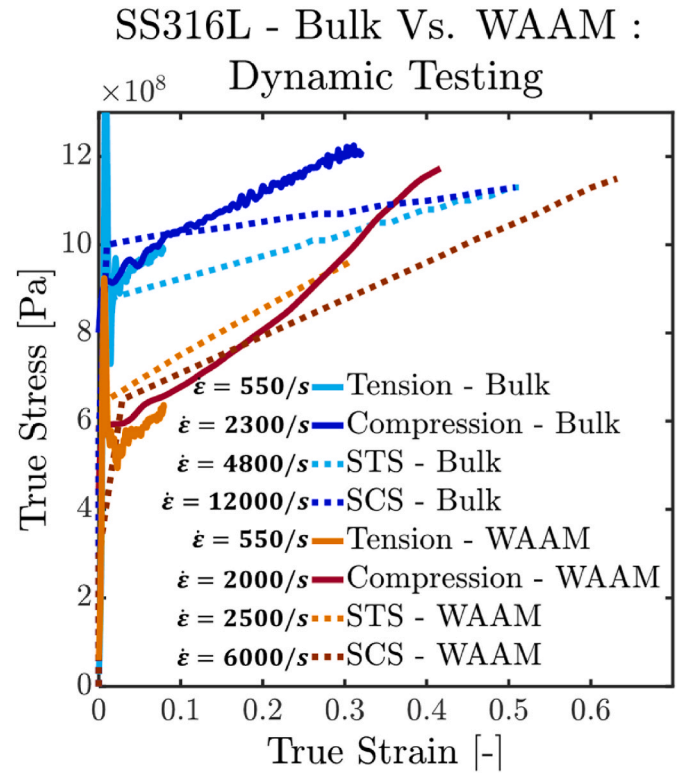


Fig. 8. Incident, reflected and transmitted average engineering strains for dynamic bulk SS316L SCS as were measured during experiments as opposed to the simulated ones after material's properties were calibrated. Good agreement can be seen between plots.



**Fig. 9.** Summary of all static experiments ( $10^{-3}$  1/s) for SS316L WAAM and bulk material in the plastic region. Errors between tested specimens of the same kind (error bars) are within 5% from the nominal presented curves. All the results are summarized in appendix A.



**Fig. 11.** Summary of all dynamic experiments for SS316L SWAAM and bulk material in the plastic region with their equivalent strain rates presented in 1/s units. Errors between tested specimens of the same kind (error bars) are within 5% from the nominal presented curves. All the results are summarized in appendix A.

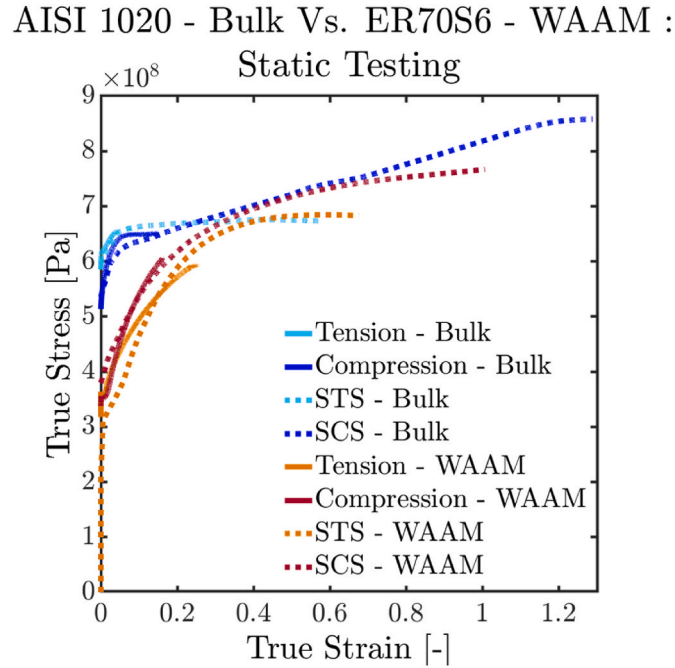


**Fig. 10.** Summary of all static experiments ( $10^{-3}$  1/s) for ER70S6 WAAM and AISI 1020 bulk materials in the plastic region. Errors between tested specimens of the same kind (error bars) are within 5% from the nominal presented curves. All the results are summarized in appendix A.

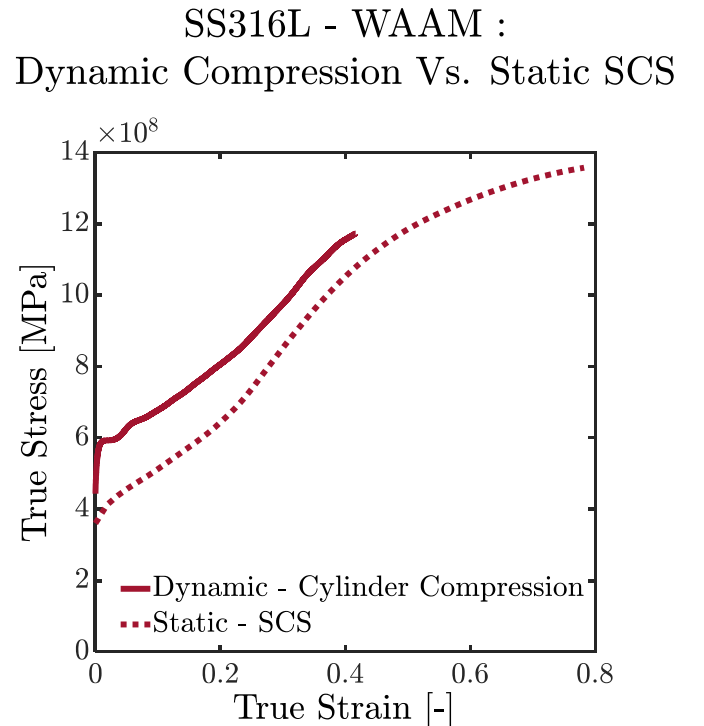


**Fig. 12.** Comparison between dynamic compression and static SCS, shows same upward concavity.

cylinder and static SCS results are plotted for comparison in Fig. 12, which suggests the operation of a similar deformation mechanism(s). However, the dynamic SCS does not show this kind of behavior.

The bulk material shows very good agreement between compression and tension and some deviation for the SCS and STS. Almost no strain hardening can be seen for the SCS, which achieved an average equivalent strain rate of 12,000 1/s.

#### 4.2.2. WAAM ER70S6 and bulk AISI 1020

All the results are presented in Fig. 13 and are summarized in appendix A. The WAAM material exhibits some difference in tensile vs. compressive yield strength which does not appear in the bulk material. A reason for that might be enhanced strain rate sensitivity for the WAAM Material. Despite the difference in the yield strength, both tension and compression curves have a similar strain hardening slope for the WAAM material as opposed to the bulk.

The WAAM STS has shown a positive strain hardening slope as opposed to bulk STS and SCS for both materials which have no strain hardening (flat curve). A reason for that is probably the lower equivalent strain rate (5550 1/s) this specimen achieved during the experiments as opposed to other shear specimens ( $10^4$  1/s and above). The flattening of the equivalent stress strain curves of all shear specimens except WAAM STS, may be related to shear localization. An example of this phenomenon can be found in the work of Vural et al. (2003), where AISI 1018 was tested (which is almost identical to AISI 1020 used in this work) under a variety of equivalent strain rates. According to their results, under low dynamic equivalent strain rates (up to 2000 1/s) the equivalent stress strain curve rises – strain hardening is present, under moderate strain rates the equivalent stress strain flattens (4000 1/s) – no strain hardening is present, and at high equivalent strain rates (around  $10^4$  1/s and above) the slope of the equivalent stress strain curve decreases – strain softening is evidenced. This effect is apparently due to shear banding or strong thermal softening at high equivalent strain rates.

### AISI 1020 - Bulk Vs. ER70S6 - WAAM : Dynamic Testing

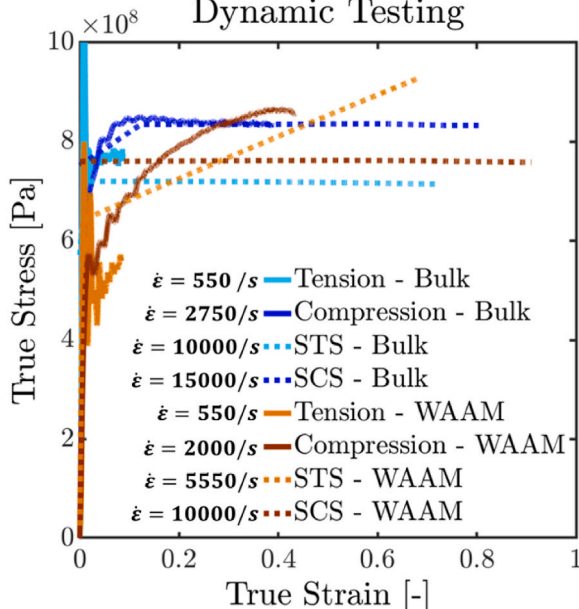


Fig. 13. Summary of all dynamic experiments ER70S6 WAAM and AISI 1020 bulk materials in the plastic region with their equivalent strain rates in 1/s units. Errors between tested specimens of the same kind (error bars) are within 5% from the nominal presented curves. All the results are summarized in appendix A.

## 5. Discussion

### 5.1. ER70S6 and SS316L

The emphasis of the presented work was to evaluate and compare the plastic macroscopic behavior of wire and arc additively manufactured (WAAM) ER70S6 and SS316L. Systematic experiments took place both at low (static) and high (dynamic) strain rates. Beside the usually used specimens of “dog-bone” for tension and cylinder for compression, shear compression specimen (SCS) and shear tension specimen (STS) were used. The use of SCS and STS enabled achievement of high equivalent strain and strain rates, in addition to the characterization of the usually overlooked shear behavior of the materials.

A good agreement was observed for different specimens with the same loading condition (static or dynamic), same material (ER70S6 or SS316L) and same manufacturing process (bulk or WAAM). Differences can be found in all cases between the bulk and WAAM materials, and such differences justify the importance of thorough mechanical properties characterization for each AM process. All the materials were used in as received condition, bulk material after cold drawing and WAAM material after a repeated cycles of warming and cooling slowly, as part of the manufacturing process (somewhat like annealing). Hence, the yield stress of the bulk material is higher as expected from an as received vs. an annealed material. Concerning work hardening behavior, the above argument applies once again. Namely, annealed (or anneal-like) materials always exhibit a higher strain hardening than their as-received (often cold-worked) counterparts.

Although a good agreement was achieved between the mixed loading conditions specimens (for STS and SCS) and the regular ones (“dog-bone” and cylinder), small deviations can be found in the yield stress with more emphasis in dynamic experiments. These small deviations can mainly be explained by differences in the strain rate and the mixed loading SCS and STS, characterized by a different triaxiality and Lode parameter conditions as opposed to standard specimens (“dog-bone” and cylinder). Triaxiality and Lode parameter are known to have an influence on the material’s equivalent stress strain behavior ((Bai and Wierzbicki, 2008; Barsoum and Faleskog, 2007a,b; Gao et al., 2009; Pivonka and Willam, 2003). Appendix A summarizes the triaxiality and Lode parameters for all experiments.

### 5.2. WAAM ER70S6 and Bulk AISI 1020

Table 1 represents a qualitative comparison for all specimens from these materials. For ER70S6 and AISI 1020, although different yield stress can be observed (probably due to the use of cold drawn bars for AISI 1020 instead of annealed material), relatively similar stress-strain characteristics were achieved for high strains. One can think of some advantages of that similarity, such as combining ER70S6 to repair defective areas at the manufacturing process of AISI 1020 products, and then plastically form the repaired material as one part, i.e., designing a process that might include material tearing on purpose at some equivalent strain, and then filling the torn places and continue plastic forming, this way achieving a much higher effective strain and formability.

### 5.3. WAAM and bulk SS316L

Table 2 represents a qualitative comparison for all specimens from these materials. The yield stress is higher for the bulk material under all conditions. Strain hardening in most cases has a bigger slope for the WAAM material which might be caused by the different microstructure, as was presented in (Ron et al., 2021; Shirizly and Dolev, 2019). The ductility is larger for the bulk material under static loading for all specimens, while for dynamic loading WAAM has a benefit for compression-based specimens.

WAAM SS316L exhibits an upper concave stress-strain behavior for static SCS, and dynamic compression experiments as opposed to bulk



**Table 1**

Qualitative comparison of the yield stress, strain hardening average slope and ductility for WAAM ER70S6 (WAAM) as opposed to bulk AISI 1020 (bulk). The indicated material indicates a higher value of the compared property while ‘ = ’ stands for similar properties.

			tension	compression	STS	SCS
WAAM and bulk SS316L	Static experiments	yield	Bulk	Bulk	Bulk	Bulk
		hardening	=	=	WAAM	WAAM*
	Dynamic experiments	ductility	Bulk	=	Bulk	Bulk
		yield	Bulk	Bulk	Bulk	Bulk
		hardening	=	WAAM*	WAAM	WAAM
		ductility	=	WAAM	Bulk	WAAM

**Table 2**

Qualitative comparison of the yield stress, strain hardening average slope and ductility for WAAM SS316L (WAAM) as opposed to bulk SS316L (bulk). The indicated material indicates a higher value of compared property, and ‘ = ’ stands for similar properties. “\*” next to WAAM emphasizes the upper concave behavior that was observed for the WAAM material.

			tension	compression	STS	SCS
WAAM ER70S6 and bulk AISI 1020	Static experiments	yield	Bulk	Bulk	Bulk	Bulk
		hardening	WAAM	WAAM	WAAM	WAAM
		ductility	WAAM	=	WAAM	Bulk
	Dynamic experiments	yield	Bulk	Bulk	Bulk	Bulk
		hardening	WAAM	WAAM	WAAM	=
		ductility	=	=	Bulk	WAAM

SS316L, and this unique behavior was not observed for all other WAAM SS316L specimens. In other words, this concavity is characteristic of compression specimens (be it uniaxial or combined with shear). The observed “S” shaped stress-strain curve for the static SCS and dynamic compression specimens does probably result from twinning, according to a previous work on the same material of SS316L but using a different AM method of powder bed fusion (PBF) instead of WAAM. Twinning above 0.3 strain was observed, which caused an improved strength and ductility as opposed to annealed SS316L bulk material (Pham et al., 2017). In our case, twinning could not be detected by both optical microscopy and SEM, and further microscopic characterization of the deformation mechanism(s) is needed that is beyond the scope of this paper. In any case, this special hardening behavior might be very important feature for e.g., plastic forming, where local hardening can prevent necking and tearing in problematic geometries like sharp edges for deep drawing.

## 6. Conclusions

WAAM SS316L is not mechanically similar to the bulk material and has its own unique behavior. This must be kept in mind when considering WAAM SS316L as a substitute for its bulk counterpart.

The unique upper-concave stress-strain behavior of the WAAM

material results most likely from twinning, usually observed for HCP materials. Although twins couldn't be detected using SEM, a thorough microstructural analysis is to be carried next for understanding the underlying deformation micromechanisms.

Increasing hardening for this material may confer additional stability during plastic forming processes.

By contrast, WAAM ER70S6 exhibits a rather similar behavior to that of AISI 1020 and can this be considered as a suitable mechanically equivalent material, under both quasi-static and dynamic loading.

## Declaration of competing interest

The authors declare that they have no known competing financial interests or personal relationships that could have appeared to influence the work reported in this paper.

## Acknowledgements

Mr. A. Reuven and Mr. Y. Rozitski's assistance with the production of the specimens and conducting the experiments is greatly appreciated. We are pleased to acknowledge many helpful discussions with Dr. A. Dorogoy on data reduction topics.

## Appendix A

A summary of yield stress, experimental strain rate, maximum achieved true strain (up to ultimate stress), triaxiality and Lode parameters are presented in Table A.1 up to Table A.4.

Triaxiality ( $t_r$ ) and Lode parameters ( $\mu$ ) were calculated according to Dorogoy et al. (2015), using the following equations:

$$t_r = \frac{P}{\sigma_e} = \frac{-\frac{1}{3}\sigma_{ii}}{\sqrt{\frac{3}{2}s_{ij}s_{ij}}} = \frac{-\frac{1}{3}(\sigma_1 + \sigma_2 + \sigma_3)}{\sqrt{\frac{1}{2}[(\sigma_1 - \sigma_2)^2 + (\sigma_1 - \sigma_3)^2 + (\sigma_2 - \sigma_3)^2]}} \quad (A1)$$

$$\mu = \frac{2\sigma_2 - \sigma_1 - \sigma_3}{\sigma_1 - \sigma_3} \quad (A2)$$

where P is the pressure,  $\sigma_e$  is the equivalent Mises stress,  $s$  is the deviatoric tensor.  $\sigma_1, \sigma_2, \sigma_3$  stands for the principal stresses when  $\sigma_1 > \sigma_2 > \sigma_3$ . More information on the triaxiality and Lode parameter definitions and influence can be found, e.g., in Barsoum and Faleskog (2007a).

## WAAM and Bulk SS316L

**Table A.1**

Summary of all WAAM 316L specimens for yield stress, strain rate, maximum strain, triaxiality and Lode parameter for all specimens and loadings.

Material	Experiment conditions	Loading regime	Specimen	Yield stress [MPa]	Strain rate [1/s]	Maximum strain [–]	Triaxiality	Lode parameter
WAAM 316L	Static	Tension	Dog-bone	330	10–3	0.22		–1
		Compression	Cylinder	350	10–3	0.18		1
		Shear - tension	STS	350	10–3	0.6	–0.38 ÷ –0.33	–0.86 ÷ –0.6
	Dynamic	Shear - compression	SCS	350	10–3	0.78	0.28 ÷ 0.32	0.35 ÷ 0.66
		Tension	Dog-bone	520	550	0.08		–1
		Compression	Cylinder	570	2000	0.42		1
		Shear - tension	STS	600	2500	0.31	–0.42 ÷ –0.35	–0.78 ÷ –0.58
		Shear - compression	SCS	650	6000	0.63	0.29 ÷ 0.42	0.58 ÷ 0.81

**Table A.2**

Summary of all Bulk 316L specimens for yield stress, strain rate, maximum strain, triaxiality and Lode parameter for all specimens and loadings.

Material	Experiment conditions	Loading regime	Specimen	Yield stress [MPa]	Strain rate [1/s]	Maximum strain [–]	Triaxiality	Lode parameter
Bulk 316L	Static	Tension	Dog-bone	730	10–3	0.26		–1
		Compression	Cylinder	690	10–3	0.16		1
		Shear - tension	STS	690	10–3	0.7	–0.42 ÷ –0.37	–0.71 ÷ –0.55
	Dynamic	Shear - compression	SCS	690	10–3	1.29	0.22 ÷ 0.35	0.42 ÷ 0.64
		Tension	Dog-bone	900	550	0.08		–1
		Compression	Cylinder	910	2300	0.32		1
		Shear - tension	STS	880	4800	0.51	–0.7 ÷ –0.59	–0.45 ÷ –0.4
		Shear - compression	SCS	1000	12,000	0.5	0.29 ÷ 0.46	0.6 ÷ 0.73

## WAAM ER70S6 and Bulk AISI 1020:

**Table A.3**

Summary of all WAAM ER70S6 specimens for yield stress, strain rate, maximum strain, triaxiality and Lode parameter for all specimens and loadings.

Material	Experiment conditions	Loading regime	Specimen	Yield stress [MPa]	Strain rate [1/s]	Maximum strain [–]	Triaxiality	Lode parameter
WAAM ER70S6	Static	Tension	Dog-bone	350	10–3	0.25		–1
		Compression	Cylinder	350	10–3	0.16		1
		Shear - tension	STS	315	10–3	0.68	–0.45 ÷ –0.31	–0.78 ÷ –0.53
	Dynamic	Shear - compression	SCS	380	10–3	1	0.25 ÷ 0.34	0.45 ÷ 0.67
		Tension	Dog-bone	470	550	0.08		–1
		Compression	Cylinder	560	2000	0.43		1
		Shear - tension	STS	640	5550	0.69	–0.45 ÷ 0.4	–0.77 ÷ –0.57
		Shear - compression	SCS	760	10,000	0.91	0.25 ÷ 0.48	0.52 ÷ 0.72

**Table A.4**

Summary of all Bulk AISI 1020 specimens for yield stress, strain rate, maximum strain, triaxiality and Lode parameter for all specimens and loadings.

Material	Experiment conditions	Loading regime	Specimen	Yield stress [MPa]	Strain rate [1/s]	Maximum strain [–]	Triaxiality	Lode parameter
Bulk ER70S6	Static	Tension	Dog-bone	590	10–3	0.05		–1
		Compression	Cylinder	540	10–3	0.15		1
		Shear - tension	STS	590	10–3	0.57	–0.48 ÷ –0.38	–0.57 ÷ –0.38
		Shear - compression	SCS	540	10–3	1.29	0.19 ÷ 0.36	0.46 ÷ 0.56
	Dynamic	Tension	Dog-bone	730	550	0.09		–1
		Compression	Cylinder	760	2750	0.39		1
		Shear - tension	STS	720	10,000	0.72	–0.54 ÷ –0.43	–0.63 ÷ –0.38
		Shear - compression	SCS	760	15,000	0.8	0.28 ÷ 0.48	0.5 ÷ 0.83

## Funding sources

This research did not receive any specific grant from funding agencies in the public, commercial, or not-for-profit sectors.

## Credit author statement

**Gleb Gil Goviazin:** Methodology, Formal analysis, Investigation, Writing – original draft, Visualization. **Amnon Shirizly:** Conceptualization, Validation, Resources, Writing – review & editing, Visualization. **Daniel Rittel:** Methodology, Validation, Resources, Writing – review & editing, Visualization, Supervision.

## References

- ABAQUS, 2014. Abaqus 6.14. Abaqus 6.14 Analysis User's Guide 14.
- Ali, U., 2012. TEZ) Numerical Modeling of Failure in Magnesium Alloys under Axial Compression and Bending for Crashworthiness Applications 96.
- Bai, Y., Wierzbicki, T., 2008. A new model of metal plasticity and fracture with pressure and Lode dependence. *Int. J. Plast.* 24, 1071–1096. <https://doi.org/10.1016/j.ijplas.2007.09.004>.
- Barsoum, I., Faleskog, J., 2007a. Rupture mechanisms in combined tension and shear-Micromechanics. *Int. J. Solid Struct.* 44, 5481–5498. <https://doi.org/10.1016/j.jisolsr.2007.01.010>.
- Barsoum, I., Faleskog, J., 2007b. Rupture mechanisms in combined tension and shear-Experiments. *Int. J. Solid Struct.* 44, 1768–1786. <https://doi.org/10.1016/j.jisolsr.2006.09.031>.
- Beese, A.M., 2018. Microstructure and mechanical properties of AM builds. In: *Thermo-Mechanical Modeling of Additive Manufacturing*, first ed. Elsevier Inc. <https://doi.org/10.1016/B978-0-12-811820-7.00007-0>.
- Ding, D., Pan, Z., Cuiuri, D., Li, H., 2015. Wire-feed additive manufacturing of metal components: technologies, developments and future interests. *Int. J. Adv. Manuf. Technol.* 81, 465–481. <https://doi.org/10.1007/s00170-015-7077-3>.
- Ding, D., Pan, Z., Dominic, C., Li, H., 2011. Process Planning Strategy for Wire and Arc Additive Manufacturing Dong-Hong, vol. 88, p. 13. <https://doi.org/10.1007/978-3-642-19959-2>.
- Dorogoy, A., Rittel, D., 2017. Dynamic large strain characterization of tantalum using shear-compression and shear-tension testing. *Mech. Mater.* 112, 143–153. <https://doi.org/10.1016/j.mechmat.2017.06.003>.
- Dorogoy, A., Rittel, D., 2005a. Numerical validation of the shear compression specimen. Part II: dynamic large strain testing. *Exp. Mech.* 45, 167–177. <https://doi.org/10.1177/0014485105052325>.
- Dorogoy, A., Rittel, D., 2005b. Numerical validation of the shear compression specimen. Part I: quasi-static large strain testing. *Exp. Mech.* 45, 167–177. <https://doi.org/10.1177/0014485105052325>.
- Dorogoy, A., Rittel, D., Godinger, A., 2016. A shear-tension specimen for large strain testing. *Exp. Mech.* 56, 437–449. <https://doi.org/10.1007/s11340-015-0106-1>.
- Dorogoy, A., Rittel, D., Godinger, A., 2015. Modification of the shear-compression specimen for large strain testing. *Exp. Mech.* 55, 1627–1639. <https://doi.org/10.1007/s11340-015-0057-6>.
- Fadida, R., Rittel, D., Shirizly, A., 2015. Dynamic mechanical behavior of additively manufactured Ti6Al4V with controlled voids. *J. Appl. Mech. Trans. ASME* 82. <https://doi.org/10.1115/1.4029745>.
- Fadida, R., Shirizly, A., Rittel, D., 2019. The static and dynamic shear-tension mechanical response of AM Ti6Al4V containing spherical and prolate voids. *Int. J. Eng. Sci.* 141, 1–15. <https://doi.org/10.1016/j.ijengsci.2019.05.003>.
- Gao, X., Zhang, T., Hayden, M., Roe, C., 2009. Effects of the stress state on plasticity and ductile failure of an aluminum 5083 alloy. *Int. J. Plast.* 25, 2366–2382. <https://doi.org/10.1016/j.ijplas.2009.03.006>.
- Kolsky, H., 1953. *Stress Waves in solids., Monographs on the Physics and Chemistry of Materials.* Clarendon Press, Oxford.
- Liberini, M., Astarita, A., Campatelli, G., Scippa, A., Montevocchi, F., Venturini, G., Durante, M., Boccardo, L., Minutolo, F.M.C., Squillace, A., 2017. Selection of optimal process parameters for wire Arc Additive manufacturing. *Procedia CIRP* 62, 470–474. <https://doi.org/10.1016/j.procir.2016.06.124>.
- Ni, X., qing, Kong, cheng, D., Wen, Y., Zhang, L., Wu, W. heng, He, B. bei, Lu, L., Zhu, D. xiang, 2019. Anisotropy in mechanical properties and corrosion resistance of 316L stainless steel fabricated by selective laser melting. *Int. J. Miner. Metal. Mater.* 26, 319–328. <https://doi.org/10.1007/s12613-019-1740-x>.
- Pham, M.S., Dovguy, B., Hooper, P.A., 2017. Twinning induced plasticity in austenitic stainless steel 316L made by additive manufacturing. *Mater. Sci. Eng.* 704, 102–111. <https://doi.org/10.1016/j.msea.2017.07.082>.
- Pivonka, P., Willam, K., 2003. The effect of the third invariant in computational plasticity. *Eng. Comput.* 20, 741–753. <https://doi.org/10.1108/02644400310488844>.
- Rittel, D., Lee, S., Ravichandran, G., 2002a. A shear compression specimen for large strain testing. *Exp. Mech.* 42, 58–64. <https://doi.org/10.1007/BF02411052>.
- Rittel, D., Ravichandran, G., Lee, S., 2002b. Large strain constitutive behavior of OFHC copper over a wide range of strain rates using the shear compression specimen. *Mech. Mater.* 34, 627–642. [https://doi.org/10.1016/S0167-6636\(02\)00164-3](https://doi.org/10.1016/S0167-6636(02)00164-3).
- Rittel, D., Zhang, L.H., Osovski, S., 2017. The dependence of the Taylor–Quinney coefficient on the dynamic loading mode. *J. Mech. Phys. Solid.* 107, 96–114. <https://doi.org/10.1016/j.jmps.2017.06.016>.
- Ron, T., Dolev, O., Leon, A., Shirizly, A., Aghion, E., 2021. Effect of phase transformation on stress corrosion behavior of additively manufactured austenitic stainless steel produced by directed energy deposition. *Materials* 14, 1–12. <https://doi.org/10.3390/ma14010055>.
- Ron, T., Levy, G.K., Dolev, O., Leon, A., Shirizly, A., Aghion, E., 2020. The effect of microstructural imperfections on corrosion fatigue of additively manufactured ER70S-6 alloy produced by wire arc deposition. *Metals* 10. <https://doi.org/10.3390/met10010098>.
- Ron, T., Levy, G.K., Dolev, O., Leon, A., Shirizly, A., Aghion, E., 2019. Environmental behavior of low carbon steel produced by a wire arc additive manufacturing process. *Metals* 9. <https://doi.org/10.3390/met9080888>.
- Shirizly, A., Dolev, O., 2019. From wire to seamless flow-formed tube: leveraging the combination of wire Arc Additive manufacturing and metal forming. *JOM (J. Occup. Med.)* 71, 709–717. <https://doi.org/10.1007/s11837-018-3200-x>.
- Tolosa, I., Garciandia, F., Zubiri, F., Zapirain, F., Esnaola, A., 2010. Study of mechanical properties of AISI 316 stainless steel processed by “selective laser melting”. *Follow. Diff. Manufact. Strat. Int. J. Adv. Manufact. Technol.* 51, 639–647. <https://doi.org/10.1007/s00170-010-2631-5>.
- Vural, M., Rittel, D., Ravichandran, G., 2003. Large strain mechanical behavior of 1018 cold-rolled steel over a wide range of strain rates. *Metall. Mater. Trans.* 34A, 2873–2886. <https://doi.org/10.1115/1.4005268>.
- Weinong Chen, B.S., 2013. *Split Hopkinson (Kolsky) Bar.* Springer, New York Dordrecht Heidelberg London.
- Wu, W., Xue, J., Wang, L., Zhang, Z., Hu, Y., Dong, C., 2019. Forming process, microstructure, and mechanical properties of thin-walled 316L stainless steel using speed-cold-welding additive manufacturing. *Metals* 9. <https://doi.org/10.3390/met9010109>.